Remote Sens. **2015**, *7*, 5828-5848; doi:10.3390/rs70505828

OPEN ACCESS

remote sensing

ISSN 2072-4292

www.mdpi.com/journal/remotesensing

Article

Using the Surface Temperature-Albedo Space to Separate Regional Soil and Vegetation Temperatures from ASTER Data

Lisheng Song [1,2], Shaomin Liu [1,*], William P. Kustas [2], Ji Zhou [3] and Yanfei Ma [1,4]

[1] State Key Laboratory of Remote Sensing Science, and School of Geography, Beijing Normal University, Beijing 100875, China; E-Mails: scausls@163.com (L.S.); mayanfei8866@126.com (Y.M.)

[2] Hydrology and Remote Sensing Lab, USDA-ARS, Beltsville, MD 20705, USA; E-Mail: Bill.Kustas@ars.usda.gov

[3] School of Resources and Environment, University of Electronic Science and Technology of China, Chengdu 611731, China; E-Mail: jzhou233@uestc.edu.cn

[4] Department of Geography, Handan College, Handan 056005, China

* Author to whom correspondence should be addressed; E-Mail: smliu@bnu.edu.cn; Tel: +86-10-5880-2240. Fax: +86-10-5880-5274.

Academic Editors: Xin Li, George P. Petropoulos and Prasad S. Thenkabail

Received: 20 January 2015 / Accepted: 29 April 2015 / Published: 8 May 2015

Abstract: Soil and vegetation component temperatures in non-isothermal pixels encapsulate more physical meaning and are more applicable than composite temperatures. The component temperatures however are difficult to be obtained from thermal infrared (TIR) remote sensing data provided by single view angle observations. Here, we present a land surface temperature and albedo (*T*-α) space approach combined with the mono-surface energy balance (SEB-1S) model to derive soil and vegetation component temperatures. The *T*-α space can be established from visible and near infrared (VNIR) and TIR data provided by single view angle observations. This approach separates the soil and vegetation component temperatures from the remotely sensed composite temperatures by incorporating soil wetness iso-lines for defining equivalent soil temperatures; this allows vegetation temperatures to be extracted from the *T*-α space. This temperature separation methodology was applied to advanced scanning thermal emission and reflection radiometer (ASTER) VNIR and high spatial resolution TIR image data in an artificial oasis area during the entire growing season. Comparisons with ground measurements showed that the *T*-α space approach produced reliable soil and vegetation component temperatures in the study area. Low root mean square

error (RMSE) values of 0.83 K for soil temperatures and 1.64 K for vegetation temperatures, respectively, were obtained, compared to component temperatures measurements from a ground-based thermal camera. These results support the use of soil wetness iso-lines to derive soil surface temperatures. It was also found that the estimated vegetation temperatures were extremely close to the near surface air temperature observations when the landscape is well watered under full vegetation cover. More robust soil and vegetation temperature estimates will improve estimates of soil evaporation and vegetation transpiration, leading to more reliable the monitoring of crop water stress and drought.

Keywords: land surface temperature and albedo space; SEB-1S; soil and vegetation component temperatures; validation; advanced scanning thermal emission and reflection radiometer (ASTER)

1. Introduction

Land surface temperature is a key parameter in the physics of land surface processes at regional and global scales; it is a metric representative of surface-atmosphere interactions and energy fluxes between the atmosphere and the ground surface [1]. Currently, satellite data offer the possibility to map land surface temperature over the entire globe effectively, with sufficiently high spatial and temporal resolution [2]. The spatially distributed land surface temperature estimated from thermal infrared (TIR) remote sensing data is widely used in studies of evapotranspiration, climate change and the hydrological cycle [3–6], soil moisture estimation [7,8], forest fire detection [9,10], vegetation water stress [11], urban heat island monitoring [12] and many other environmental monitoring applications. Passive microwave (PW) remote sensing can also provide land surface temperature observations [13], which is unaffected by clouds. However, the satellite based PW sensors have very coarse spatial resolutions compared with the thermal infrared (TIR) remote sensing. In addition, estimation of land surface temperature from the PW have limitations associated with restricted response depth and producing more uncertainties over barren and sparse vegetation covered land surfaces compared to TIR, which is commonly used in modeling evapotranspiration [14]. In a heterogeneous and non-isothermal pixel, however, the radiance observed by the remote sensor at the top of atmosphere (TOA) is the ensemble radiance of several components (*i.e.*, sunlit and shaded soil and vegetation) [2] so the pixel-average temperature cannot reveal the real temperature of each component, particularly in the sparse vegetation-covered arid and semi-arid areas where the soil and vegetation component temperatures are usually significantly different. Additionally, the component temperatures of a mixed pixel encapsulate more physical information than the composite temperature that relate to soil and vegetation heat fluxes and hydrologic states [2]. By deriving component soil and vegetation temperatures, the accuracy of surface fluxes estimated by two-source (soil + vegetation) energy balance models should improve capabilities to monitor crop water stress and drought, estimate surface soil moisture and result in more accurate weather forecasts [5,8,11,15,16].

The task of retrieving the component temperatures, however, is difficult, due to the variability in the distribution of internal components and the definition of effective emissivity and thermal anisotropic radiation regimes in forward processes of TIR remote sensing data. Currently, studies of soil and

vegetation component temperatures retrieval have concentrated on two aspects: multi-angular observation and multi-visible and near infrared (VNIR) and TIR band optimization. The multi-angular method generally establishes a model for reflecting the thermal infrared radiation in a continuous vegetation distribution but non-isothermal mixed pixel according to the thermal anisotropic radiation regimes. It then applies the Monte Carlo method to simulate the relationship between the component effective emissivities and variables. Through the aforementioned step, at least two equations including the parameters of soil and vegetation temperatures are established, and the soil and vegetation component temperatures are retrieved combining thermal infrared data observed by multi-angular sensors such as the Along Track Scanning Radiometer (ATSR), ATSR2, Advanced ATSR, and some airborne multi-angular thermal infrared systems [11,15,17–19]. However, the multi-angular methods may not provide accurate enough component temperatures for reliable component flux estimation. In addition, the different viewing zenith angles correspond to different pixel resolution, which means the various viewing angles are sampling a different size footprint of the land surface [2,20]. Although the different image spatial resolutions can be converted to the same level using pixel resizing and re-sampling methods, the radiation received by the sensor at these two viewing angles reflect a different land surface contribution [2,21]. Unfortunately, ATSR has been out of operation for over 10 years and its successor, the Advanced ATSR, provided data until 2012. Since then, dual-angle observations in thermal infrared have not been available.

The multi-VNIR and TIR band optimization method usually applies the ancillary information provided by the VNIR remote sensing data to obtain component fractions of soil and vegetation. The soil and vegetation component temperatures are then simulated using an optimized algorithm or Bayesian theorem from TIR remote sensing data. However, the correlations between the neighboring TIR channels cannot be neglected when applying the optimization method, which always leads to ill-posed equations with solutions that are relatively unstable [16]. In addition, the utilization of spatial dependences among adjacent pixels decreases the spatial resolution of the initial TIR images [16], and the spatial resolution of the TIR channels is usually much coarser than the VNIR pixels.

In recent years, the surface temperature-vegetation (T-f_{vg}) and surface temperature-albedo (T-α) spaces have been successfully applied to estimate surface evaporative fraction [22] and evapotranspiration [23] to disaggregate the land surface temperature and surface soil moisture [7,24–26]. Moreover, in T-f_{vg} and T-α space, surface soil wetness iso-lines can be generated [27,28]. Assuming a relatively uniform soil texture over the image, the soil temperature values for all pixels along the soil moisture iso-line are presumed to be equivalent, as are the vegetation temperature values [29–31]. The soil and vegetation component temperatures are invariant, and the land surface temperatures thus vary only with the vegetation fraction cover or the surface albedo. Therefore, if one of the equivalent temperatures can be derived, the other then can be calculated using the Stefan-Boltzmann law for the soil and vegetation system while neglecting the scale affection in the non-isothermal pixels.

The main objective of this study is to develop a practical method for separating the soil and vegetation component temperatures based on the T-α space according to the mono-surface energy balance (SEB-1S) model described below. ASTER data are used to test the method having a single viewing angle observation with high spatial resolution. The method is validated with ground component temperature measurements and evaluated based on the theory of equal soil and vegetation temperatures along the soil wetness iso-lines. Finally, some suggestions on how to validate retrieved soil and vegetation component temperatures from satellite observations are presented.

2. Study Area and Datasets

2.1. Study Area and Meteorology Data

The Heihe Watershed Allied Telemetry Experimental Research (HiWATER) program supports watershed-scale eco-hydrological experiments designed from an interdisciplinary perspective to address complex problems related to impacts of heterogeneity, scaling, and uncertainty in closing the water cycle [32]. One of the three key experimental areas of HiWATER is located in the middle reaches of Heihe, which is an artificial oasis ecosystem containing irrigated agriculture along with wetland and desert components. The first thematic experiment launched in HiWATER was the Multi-Scale Observation Experiment on Evapotranspiration over heterogeneous land surface (HiWATER-MUSOEXE). This experiment involved a flux observation matrix including a network of 21 flux towers deployed over oasis-desert surfaces in the middle reach of the Heihe River Basin from May to September in 2012 [33]. In this study, the upwelling and downwelling longwave radiation measured from the four-conponent radiometers installed at the flux towers are collected to compute land surface temperature for validating the land surface temperature retrieved from ASTER TIR data. Combining the uncertainty or error in sensor calibration, assumed emmissivity, and the spatial heterogeneity, the uncertainty in site-specific land surface temperature is likely to be on the order of 1.0 K [34]. At these sites, meteorological, soil and vegetation parameters, e.g., fraction of vegetation coverage, soil temperatures and moistures at multiple depths were measured. Soil and vegetation component emissivities were estimated using FT-IR spectrometer (102 F) measurements applied to the Iterative Spectrally Smooth Temperature Emissivity Separation (ISSTES) algorithm. The composite emissivity was computed from the measured soil and vegetation component emissivities based on fractional vegetation cover estimates. In addition, a Fluke Ti55 thermal infrared camera was manually operated on a 25-m-high platform on a flux tower at site 15 (Daman superstation, presented in Figure 1 to measure the thermal radiation of the cropland during the HiWATER experiment. The images including VNIR and TIR were recorded by the camera. Then, the soil and vegetation component temperatures were calculated according to the fraction of vegetation and soil viewed by the camera based on the VNIR data [35]. Due to a lack of other reliable independent observations of soil and vegetation temperatures, the component temperatures measured from the thermal infrared radiometers were converted to composite surface temperature and then compared to the hemispherical observations from the tower-based four-component radiometer [36]. A mean bias of 0.6 K and a root mean square error of 1.67 K was obtained, with the bias indicating a tendency for the thermal-infrared sensors to estimate a higher temperature compared to the hemispherical temperature from the four-component radiometers. Finally, the atmospheric profiles including air pressure, mean air temperature, mean air humidity, visibility and elevation were collected from the meteorological station in Zhangye City on DOY 167, 176, 192, 215, 224, 231, 240, 247 and 256.

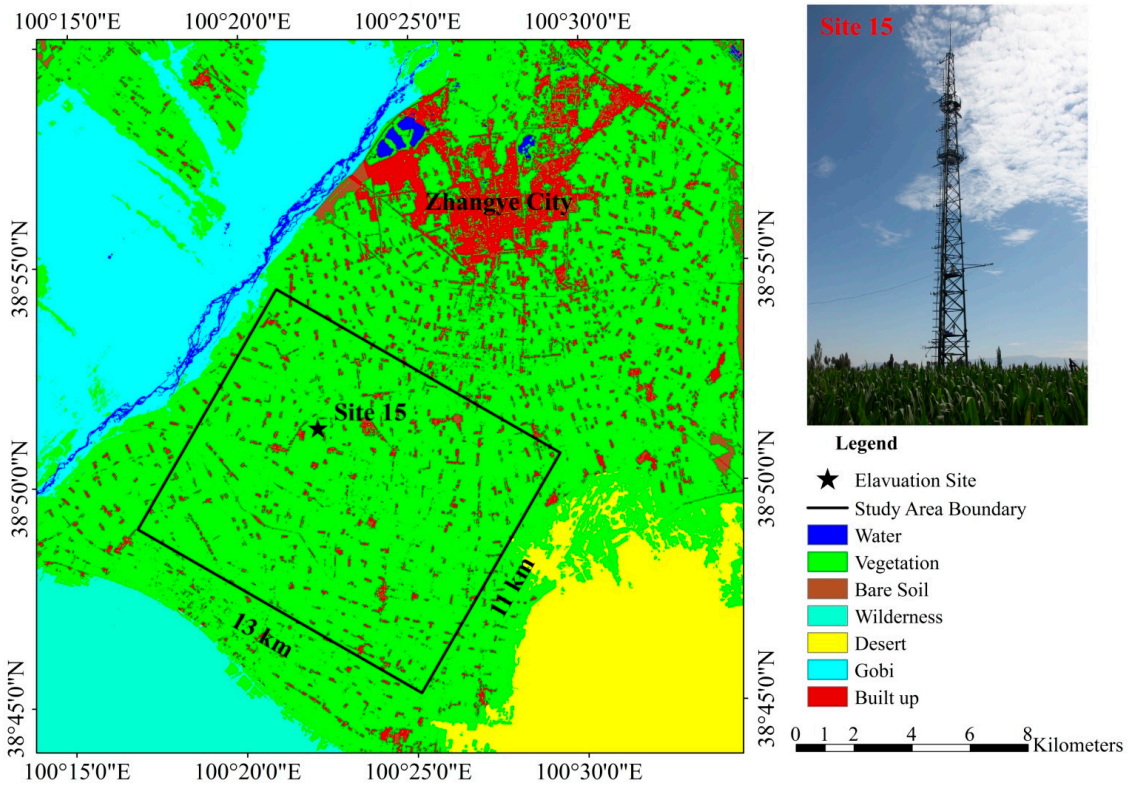

Figure 1. Spatial distribution and ground photographs of the six vegetation surface sites in this study. The upper left image is the landscape of the experimental HiWATER-MUSOEXE area, and the study area is the black rectangle with a length of 13 km and a width of 11 km.

2.2. Determination of Input Remote Sensing Data

2.2.1. Fraction of Vegetation Cover and Surface Emissivity

The fraction of vegetation cover (f_c) is calculated from the normalized difference vegetation index (NDVI) values, which are estimated from the surface reflectances of ASTER bands 2 and 3 with pixel resolution of 15 m. The reflectances are obtained through the image atmospheric correction using the MODTRAN model. The value of f_c is calculated from the following equation [37–39]:

$$f_c = \frac{NDVI - NDVI_{\min}}{NDVI_{\max} - NDVI_{\min}} \quad (1)$$

where $NDVI_{\min}$ represents the normalized vegetation index of bare soil, and $NDVI_{\max}$ represents the maximum value of the normalized vegetation index. However, the spectral signature of land surface varies due to factors including mineralogy, moisture content and grain size, and also those associated with differences in species, plant health, leaf water content, and other factors [40]. Most of $NDVI_{\min}$ and $NDVI_{\max}$ values need local calibration [37–39]. In this study, $NDVI_{\min}$ and $NDVI_{\max}$ were calculated from the 2nd and more than 95th percentiles of the statistical NDVI histogram of the study area image, respectively [39]; the $NDVI_{\min}$ values were set to 0.05, while the $NDVI_{\max}$ were set to 0.85 for the study area.

Although ASTER standard products of LST and emissivity have been widely used, significant uncertainty in the Temperature and Emissivity Separation algorithm often occurs in areas of high and low spectral contrast [41], which could introduce relative large errors in LST estimation. In addition,

uncertainty from the atmospheric corrections also leads to errors in LST estimation. Here, a hybrid procedure was utilized to estimate the surface emissivity from the ASTER image using the NDVI Thresholds Method-NDVI^{THM} in this study [42] and applying the radiative transfer algorithms with atmospheric profiles measured from Zhangye Meteorological Observation radiosondes at ASTER overpassed time [43]. The NDVI^{THM} method obtains the surface emissivity considering different cases:

(a) NDVI < 0.2, here the pixels consist of bare soil. The surface emissivity values can be calculated from the surface reflectivity (ρ_{red}) in the red channel:

$$\varepsilon = 1 - \rho_{red} \tag{2}$$

(b) NDVI > 0.5, here, the pixels are considered fully vegetated, and the surface emissivity distribution is calculated from *in situ* measurements of vegetation emissivity.

(c) 0.2 ≤ NDVI ≤ 0.5, here, the given surface is considered as a mixture of bare soil and vegetation. The emissivity of a heterogeneous surface is then expressed as [39]

$$\varepsilon = \varepsilon_c f_c + \varepsilon_s (1 - f_c) + d\varepsilon \tag{3}$$

In Equation (3), ε_c and ε_s are the emissivities of full vegetation and bare soil, respectively, which were calculated from *in situ* measurements [39] and f_c is the fraction of vegetation cover. The term $d\varepsilon$ is given as:

$$d\varepsilon = (1 - \varepsilon_s)\varepsilon_c F(1 - f_c) \tag{4}$$

where F is a shape factor whose value depends on the geometrical structure of the vegetation, the mean value is 0.55.

2.2.2. Land Surface Temperature

Using the aforementioned land surface parameter of surface emissivity and the atmospheric parameters including upwelling and downwelling radiance and transmittance, the atmospheric correction method based on the radiative transfer equation is then applied to estimate the land surface temperature [43]. The following expression of the simplified radiative transfer equation was applied to the thermal infrared images:

$$L_{sensor,\lambda} = B_\lambda(T)\varepsilon_\lambda\tau_\lambda + L_\lambda^{\uparrow} + (1 - \varepsilon_\lambda)L_\lambda^{\downarrow}\tau_\lambda \tag{5}$$

where $L_{sensor,\lambda}$ is the radiance at the top of atmosphere (TOA; the value after radiation calibration) in $Wm^{-2}\cdot sr^{-1}\cdot\mu m^{-1}$; ε_λ is the land surface emissivity; $B_\lambda(T)$ is the radiance emitted by a blackbody at temperature T, where T is in K and $B_\tau(T)$ is in $Wm^{-2}\cdot sr^{-1}\cdot\mu m^{-1}$; $L_\lambda^{\uparrow}$ and $L_\lambda^{\downarrow}$ are the atmospheric downwelling and upwelling radiances in $Wm^{-2}\cdot sr^{-1}\cdot\mu m^{-1}$, respectively; and τ_λ is the atmospheric transmittance. Atmospheric radiative transfer models (e.g., LOWTRAN and MODTRAN codes) are often used to calculate τ_λ, $L_\lambda^{\uparrow}$ and $L_\lambda^{\downarrow}$ if simultaneous atmospheric profiles are available.

The land surface temperatures retrieved from the ASTER TIR data with pixel resolution of 90 m, were compared to that calculated from the upwelling and downwelling long-wave radiation measured by four-component radiometer in the tower sites or calculated from the measured air temperature and relative humidity while the flux tower without four-component radiometers in the study area during the HiWATER-MUOEXE. The results indicate that the ASTER land surface temperatures for the selected overpass dates (DOY 167, 176, 192, 215, 224, 231, 240, 247 and 256) are in acceptable agreement with

the ground observations having an average bias of −1.12 K and an average root mean square error (RMSE) value of 2.25 K.

2.2.3. Land Surface Albedo

Land surface albedo was estimated as a linear combination of ASTER waveband reflectances. Due to deficient shortwave infrared channels since 2008, we computed the surface albedo only using the visible and near infrared channels according to the method proposed by Liang (2000) [44]. The non-snow/ice surface albedo computation formulation was given as following:

$$\alpha = 0.0771\alpha_1 + 0.3652\alpha_2 + 0.4086\alpha_3 + 0.0178 \quad (6)$$

where α_1, α_2 and α_3 are the surface albedos of the visible and near infrared channels, respectively. The ASTER broadband albedo showed good agreement with the ground observations for the 19 sites where the four-component radiometers were installed (Figure 2), with a mean bias (overestimate) of 0.004, a mean absolute percent difference of 2.6% and an RMSE value of 0.013. This result supports the use of the ASTER broadband albedo for the *T*-α space method.

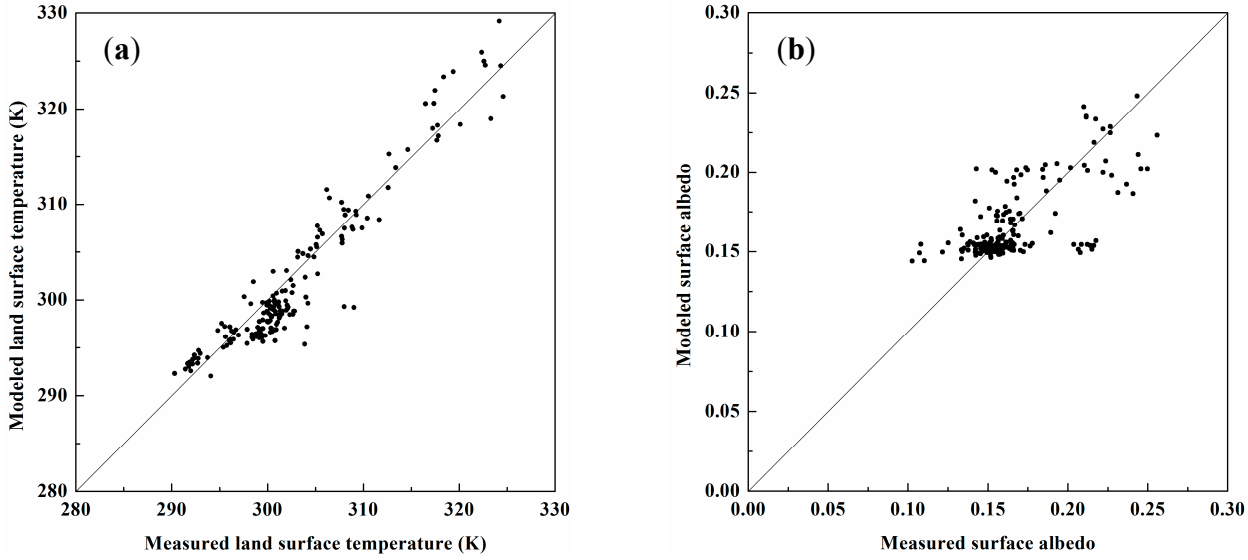

Figure 2. Comparison between the modeled and measured land surface parameters, (**a**) is land surface temperature and (**b**) is surface albedo

3. Methodology

3.1. Methods for Estimating Soil and Vegetation Component Temperatures

In this study, the separation of the soil and vegetation component temperatures for a pixel is based on the theory of the soil wetness iso-line in the *T*-α space according to the SEB-1S model [25]. Figure 3a illustrates the *T*-α space, and concepts of surface soil moisture isopleths and the temperature and albedo end-members. Figure 3b shows the procedures used to decompose composite temperatures (*T*) into soil temperature (T_s) and vegetation temperature (T_c). In the *T*-α space, the dry edge (Figure 3, red line) is generally interpreted as representing the limiting conditions of soil moisture or evapotranspiration. In

contrast, the wet edge (Figure 3, blue line) represents potential evapotranspiration [45]. The study area used to evaluate the *T*-α space approach is approximately 150 km^2 and is an irrigated cropland (primarily corn) located in a strongly adevective arid region with flat terrain (an artificial oasis). Superimposed in Figure 3a, are the soil wetness iso-lines, and it is assumed that all pixels which pass through the same iso-line have the same T_s, allowing derivation of T_c [28–30]. In the *T*-α space, the intersection of the iso-line and bare soil line is T_s, while for T_c, the value was derived from the intersection of the iso-line and the full vegetation cover line.

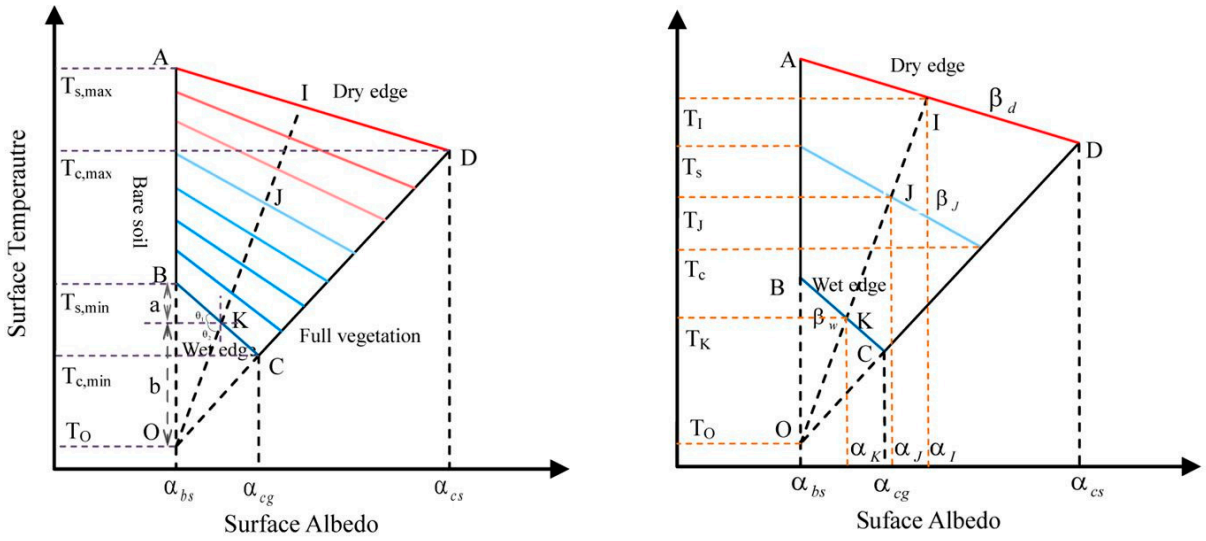

Figure 3. A sketch of the polygon *T*-α space involved in soil and vegetation component temperature separation. Points A and D pass through the dry line, and points B and C pass through the wet line according to SEB-1S model. The lines AB and CD represent the bare soil surface and fully vegetated surfaces, respectively. Slanting straight lines represent superimposed isopleths of soil moisture availability, which increase from dry edge to wet edge. (**a**) illustrates temperature and albedo end-members in the *T*-α and (**b**) illustrates the separation of soil and vegetation component temperatures from composite temperatures.

To determine the position of the *T*-α space in Figure 3, the value of seven end-members in the *T*-α space are required: The maximum soil temperature ($T_{s,max}$), the minimum soil temperature ($T_{s,min}$), the maximum vegetation temperature ($T_{c,max}$), the minimum vegetation temperature ($T_{c,min}$), the wet soil albedo (α_s), the green vegetation albedo (α_{vg}) and the senescent vegetation albedo (α_{vs}). The study area is irrigated farmland with relatively uniform atmospheric conditions and the images were collected from the early crop growing season through senescence and included DOY 167, 176, 192, 215, 224, 231, 240, 247 and 256. Consequently, this image set can provide estimates of the seven end-members in the application of the T-α space approach [7,24–26]. The end-members of albedo are set to $\alpha_s = 0.10$, $\alpha_{vg} = 0.17$, $\alpha_{vs} = 0.32$, and the temperature end-members are estimated by the synergy between *T*-α and *T*-f_{vg} spaces based on the procedure developed by Merlin *et al.* [7,23,24].

With the aforementioned analysis, for a given pixel point (*J*) along a random soil wetness iso-line in the *T*-α space, its soil temperature can be calculated based on the law of tangents:

$$(\alpha_s - \alpha_J)\beta_J + T \tag{7}$$

In Equation (7), α_s, T_s, T and α_J are the wet soil albedo, soil temperature, surface temperature and albedo of point *J*, respectively. β_J is slope of the iso-line line going across point *J*, which can be derived by interpolating the slope of the wet edge (β_w) and that of the dry edge (β_d). β_w is the ratio of the differences between $T_{s,max}$ and $T_{c,max}$ and between α_s and α_{vs}. Similarly, β_d is the ratio of the differences between $T_{s,min}$ and $T_{c,min}$ and between α_s and α_{vg}:

$$\beta_J = \frac{IJ}{IK}(\beta_d - \beta_w) + \beta_d \tag{8}$$

$$\beta_d = \frac{T_{s,\max} - T_{v,\max}}{\alpha_s - \alpha_{vs}} \tag{9}$$

$$\beta_w = \frac{T_{s,\min} - T_{v,\min}}{\alpha_s - \alpha_{vg}} \tag{10}$$

$$IJ = \sqrt{(\alpha_J - \alpha_I)^2 + (T_J - T_I)^2} \tag{11}$$

$$IK = \sqrt{(\alpha_K - \alpha_I)^2 + (T_K - T_I)^2} \tag{12}$$

The bare soil line (AB) and the full vegetation covered line (CD) cross each other at *O* (α_0, T_0), and, according to the linear interception of the iso-line in the *T*-α space, the surface temperature and albedo of the pixel *K* (α_k, T_k) on the full wet line can be obtained,

$$\alpha_O = \alpha_s \tag{13}$$

$$T_O = T_{v,\min} - \frac{\alpha_{vg} - \alpha_s}{\alpha_{vs} - \alpha_{vg}}(T_{v,\max} - T_{v,\min}) \tag{14}$$

$$\tan\theta_1 = \frac{a}{\alpha_K - \alpha_s} \tag{15}$$

$$\tan\theta_2 = \frac{b}{\alpha_K - \alpha_s} \tag{16}$$

$$\alpha_K - \alpha_s = \frac{a+b}{\tan\theta_1 + \tan\theta_2} \tag{17}$$

$$\alpha_K = \frac{a+b}{\tan\theta_1 + \tan\theta_2} + \alpha_s \tag{18}$$

$$T_K = T_{s,\min} + \beta_w(\alpha_K - \alpha_s) \tag{19}$$

$$\tan\theta_1 = \beta_{OJ} \tag{20}$$

$$\tan\theta_2 = -\beta_{wet} \tag{21}$$

$$a + b = T_{s,\min} - T_o \tag{22}$$

The surface temperature and albedo of the pixel *I* (α_1, T_1) on the full dry line:

$$\alpha_I = \frac{T_{s,\max} - T_O}{\beta_{OJ} - \beta_d} + \alpha_s \tag{23}$$

$$T_I = T_{s,\max} + \beta_d(\alpha_I - \alpha_s) \tag{24}$$

where O (α_0, T_0) is the auxiliary point on the extension of AD and IJ, a, b, θ_1 and θ_2 are the ancillary parameters (see Figure 3), and the slope of the IJ is given by the following equation,

$$\beta_{OJ} = \frac{T_J - T_O}{\alpha_J - \alpha_s} \tag{25}$$

When neglecting the scale affection in the non-isothermal pixels, based on the Stefan-Boltzmann law for the soil and vegetation system, the T_c in the pixel J can then be expressed as [36,46]:

$$T_c = \left\{ \frac{\varepsilon T_J^4 - (1 - f_c)\varepsilon_s T_s^4}{f_c \varepsilon_c} \right\}^{1/4} \tag{26}$$

3.2. Validation Procedure

To validate the estimated soil and vegetation component temperatures, this study used the ground measurements of soil and vegetation component temperatures from the thermal camera. The performance of the approach in reproducing soil and vegetation component temperatures was evaluated using two statistical measures, one was computing a bias between the component temperatures derived from the approach using the ASTER images and the ground measured component temperatures from the thermal camera is computed as:

$$bias = T_{separated} - T_{observed} \tag{27}$$

where $T_{\text{separated}}$ is the soil and vegetation component temperature separated from the ASTER data using the proposed method in this study, and T_{observed} is the observed temperatures including soil and vegetation temperatures. The second statistical measure was computing a root mean square error (RMSE) using the following equation:

$$RMSE = \frac{1}{N}\sqrt{\sum_{i=1}^{N}(T_{separated} - T_{observed})^2} \tag{28}$$

where N is the total number of observations. In addition, as mentioned earlier, the soil temperatures are equal along the soil wetness iso-lines, as are the vegetation temperatures, which mean the component temperatures along these lines should be identical as the surface albedo varied. This is evaluated qualitatively with the factors including scopes of the lines consisted by the points and the fluctuation of points in the scatter plots of soil or vegetation temperature and surface albedo.

4. The Temporal and Spatial Variability of the Soil and Vegetation Temperatures

The two-dimensional plots of surface temperature-albedo throughout the growing season over the research site were derived from the nine scenes (see Figure 4). In the plots, $T_{\text{s,max}}$ and $T_{\text{c,max}}$ refer to the maximum soil temperature and minimum canopy temperature which were derived from maximum and minimum land surface temperatures, respectively, retrieved from the ASTER thermal images in the

study area. However, the minimum soil temperature ($T_{s,min}$) and maximum canopy temperature ($T_{c,max}$) are the average values, which are computed from the two-dimensional plots according to the aforementioned procedure. According to Figure 4, it is clearly seen that these points vary considerably over the course of the season. The values of the four temperature end-members declined from the early season toward the later season, and the population of points moved gradually towards the x-axis except on DOY 240. In addition, the position and magnitude of the temperature end-menbers are closely related to changes in vegetation phenology over the course of the growing season. In conclusion, the correlation of the surface temperature-fractional cover and surface temperature-albedo spaces significantly enhances the capability to accurately derive the temperature end-members phenological changes.

The soil and vegetation component temperatures were successfully separated using the *T*-α space method in the study area from the early season to the later season (DOY 167, 176, 192, 215, 224, 231, 240, 247, 256) using the ASTER image data (Figure 5).

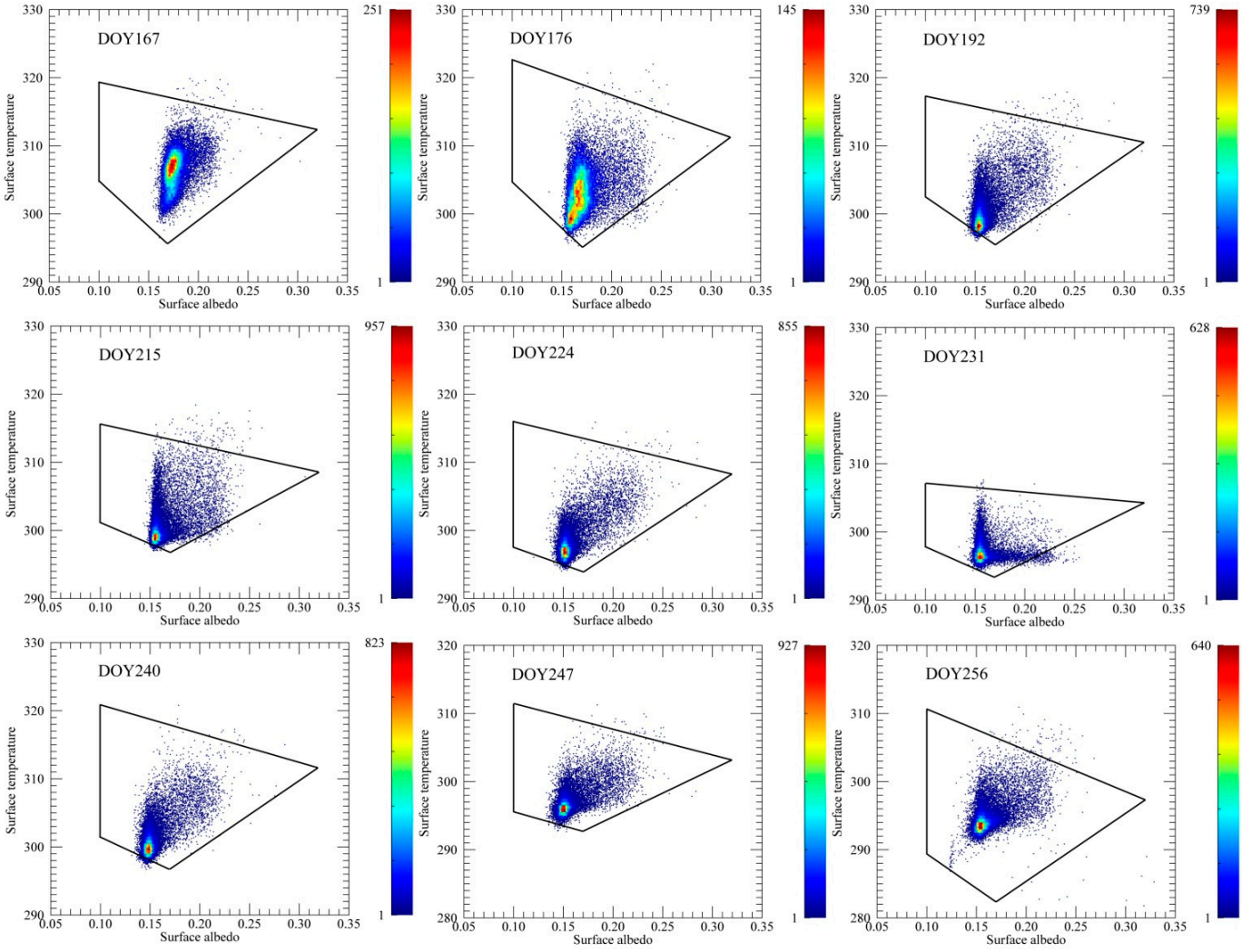

Figure 4. The spaces of surface temperature-albedo and surface temperature-green vegetation fraction, the position of dry edges, wet edges, bare soil and the full vegetation cover edge in the spaces, established by using nine senses ASTER images.

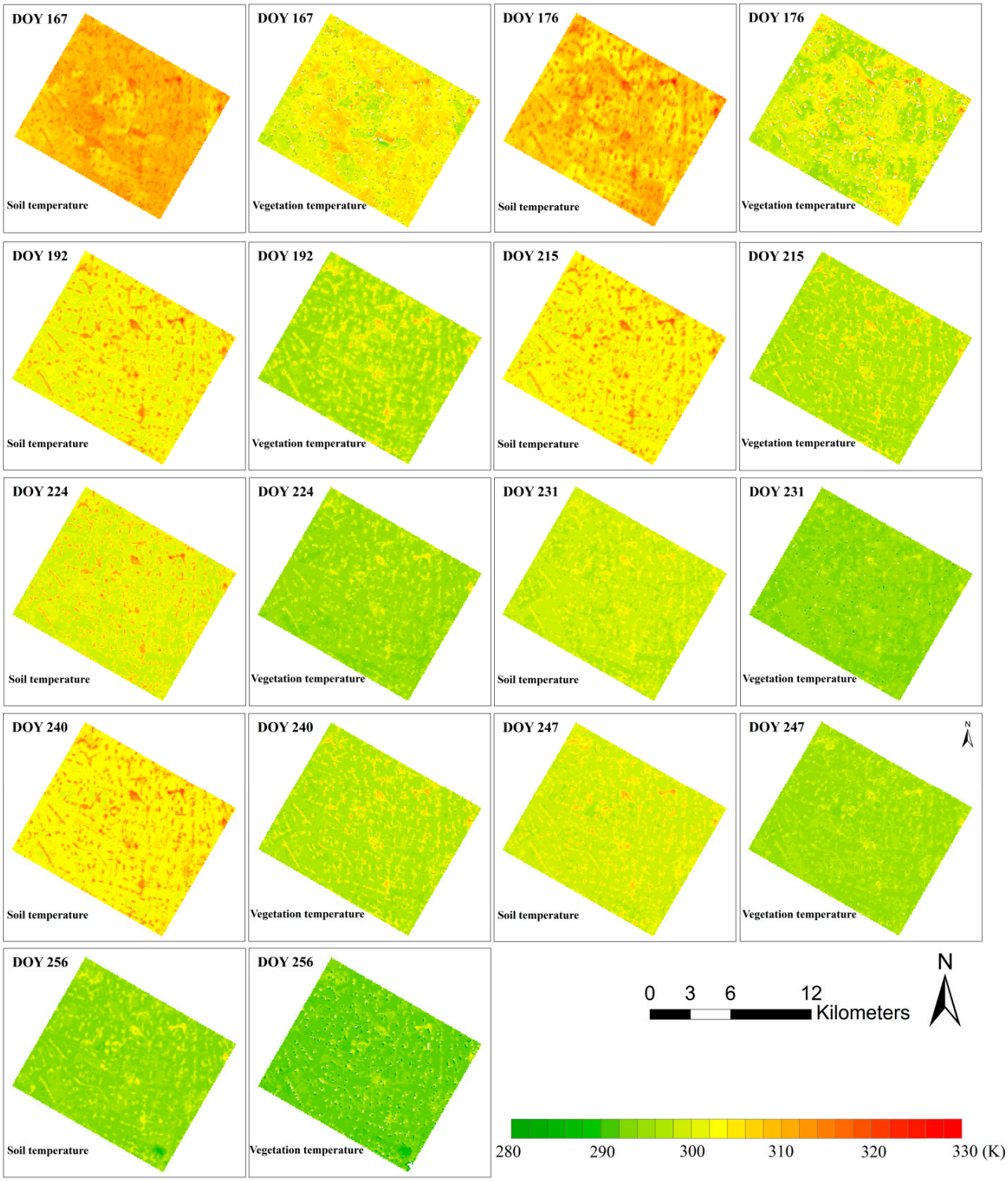

Figure 5. The spatial distribution of soil and vegetation component temperatures from nine ASTER images during the growing season.

Obviously, the temporal and spatial distribution of the soil temperature and vegetation temperatures demonstrated a cooling-down process during the growing season, with the exception of DOY 240. Furthermore the variation has good consistency with maize phonological period in the oasis, the land surface temperature is higher in the early season when the plant start to grow and stable and medium in the mid-season when the fields are nearly full covered with vegetation. There is a high spatial

heterogeneity not only of the soil temperature but also of the vegetation temperature during the early season when the row crops were partial canopy cover conditions, especially on DOY 167 and 176. The spatial variability of temperatures including soil and vegetation in the early season can be attributed to the different sowing dates of the crop, in which the different sowing dates contributed to the variation fraction canopy cover. This in turn leads to spatial variation in photosynthesis, water use and fraction of incoming solar radiation of the soil surface. Irrigation was scheduled on different days in the various fields during the four times periods with flood irrigation during the growing season. This means that the soil moisture content for the various fields differed when the satellite passed over the study area. The compounding effects from the spatial heterogeneity of the soil moisture content and the fractional vegetation cover contribute to the spatial variation in soil and vegetation component temperatures derived from the ASTER TIR images in the early growing season. However, when crops were near full canopy cover condition in the mid and late of crop growing season, the spatial distribution of the separated soil and vegetation component temperatures gradually became homogenous, especially on the DOY 231, 240 and 247, where the values of the vegetation temperature were nearly uniform over the croplands. In addition, with the fields at nearly full canopy cover, the soil below the canopy received little radiation and hence the soil temperature was fairly homogeneous.

5. Results and Validation

5.1. Validation with Ground Component Temperature Measurements

In this study, ground component temperature measurements were used to validate the instantaneous soil and vegetation component temperatures from the ASTER images. Using a high-resolution thermal camera over heterogeneous surfaces can allow the acquisition of the soil and vegetation component temperatures including sunlit and shaded soil and vegetation temperatures over land surface areas exceeding 500 m^2. However, because the soil and vegetation temperatures were manually observed on the ground, their measured times cannot exactly match satellite overpass times. The surface soil and vegetation temperatures at the specific times of satellite overpass were interpolated from the ground observed data and the diurnal temperature cycle (DTC) model [47,48]. The simulated temperatures agreed well with the observed temperatures at specific manual measurement times (Figure 6), indicating that the simulated temperatures can be applied to validate the separated soil and vegetation component temperatures when the timely ground observed data are absent.

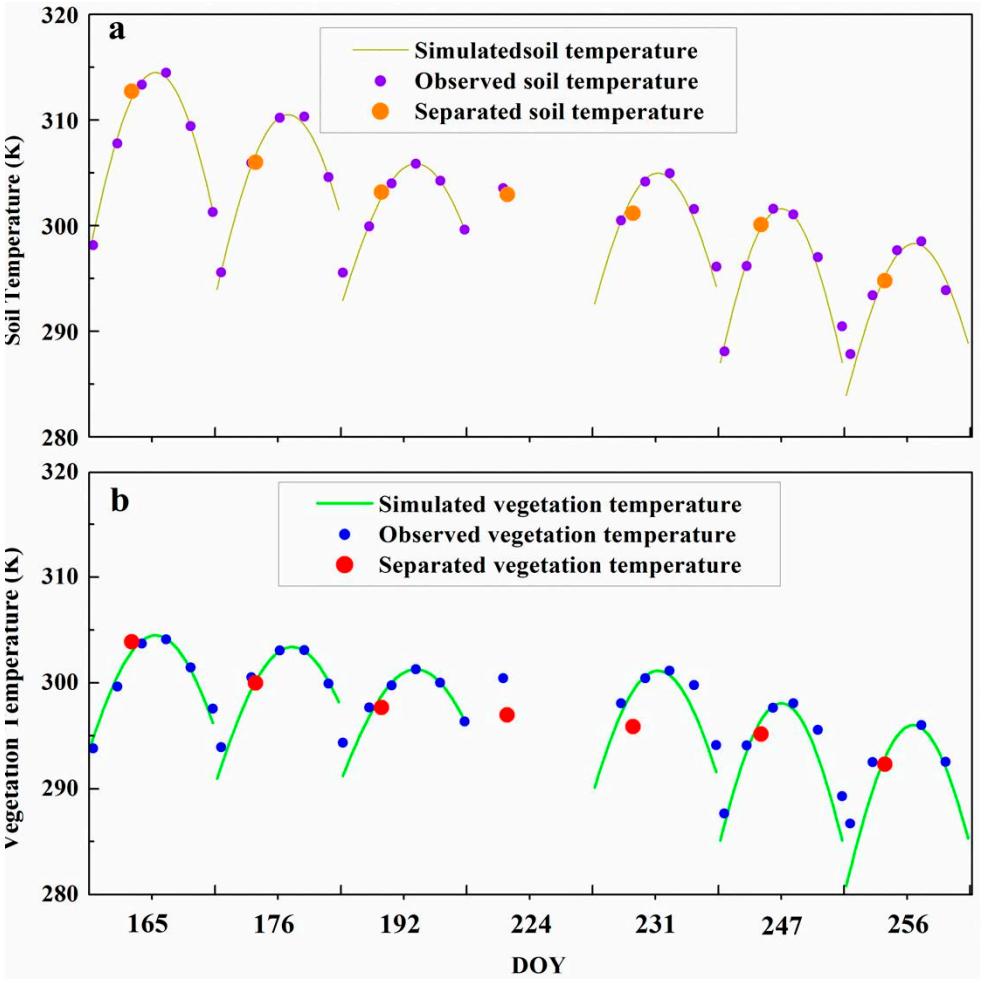

Figure 6. The interpolation of daytime surface soil temperatures (**a**) and vegetation temperatures (**b**) validated with the observed temperatures.

The performance of the proposed *T*-α space approach was validated with the interpolated ground-based soil and vegetation temperatures. Figure 6 shows the comparisons among the separated component temperatures, the ground measurements from the thermal cameras and the simulated data from multiple daytime ground measurements. There is a good agreement in the component temperatures derived from the ASTER images using the *T*-α space approach when compared with the measured soil and vegetation component temperatures, with the exception of the significant underestimation of the vegetation temperature on DOY 224 and 231. The errors in vegetation temperature on these days are due to the underestimation of land surface temperatures from the ASTER TIR data by more than −1.7 K, compared to the measured land surface temperatures calculated from the four-component radiometers and meteorological observations and computed composite emissivity. Further error analysis shows that the bias for the soil temperature ranges from −1.68 to 0.67 K, with an average of −0.27 K and an RMSE value of 0.83 K, and the bias of the vegetation temperatures range from −3.46 to 0.95 K, with an average of −1.29 K and an RMSE of 1.64 K, compared with the measured/interpolated component temperatures from the thermal camera. These errors are tolerable and comparable for soil and vegetation component temperatures separated using the *T*-α space method from the ASTER images, even though the soil and vegetation component temperatures are both underestimated.

For this study area it appears that the component temperatures from the ground-based thermal camera are in good agreement with soil and canopy temperatures derived from the *T*-α space using ASTER images having 90 m pixel resolution. Underestimated land surface temperature from the satellite will lead to underestimates of the component temperatures, so it is important to have accurate land surface temperatures compared to the ground measurements associated with the underestimations of both separated soil and vegetation temperatures [35]. Finally, the accuracy in deriving soil temperature is higher than vegetation temperature. Relatively large errors were found for vegetation temperature estimates, especially on DOY 224 and 231 (Figure 6b), which were caused by an underestimate in land surface temperature from the satellite. Increased errors in estimating vegetation temperatures may be due in part to errors in estimated fraction of vegetation cover, which is most significant during the growing period when canopy cover is less than 75%. In addition, there may be errors from the fraction of vegetation cover and neglecting the scale affection in the non-isothermal pixels when using Equation (26).

5.2. Evaluation with Existing Soil Wetness Iso-Lines

According to the approach assumption, the soil temperatures for all of the pixels along the iso-line of equal water availability in the *T*-α space are equivalent and are also similar for vegetation temperature. The basic theory of soil wetness iso-line is appropriate for the croplands in the oasis of Zhangye City, which are fully irrigated. The irrigated region mainly covers an area of 11 km × 13 km and there are more than 30,000 thermal-IR pixels; however, the wetness iso-lines have a wide range in value, from near zero to on the order of hundreds. Thus, there were only a few pixels to define the water stress iso-line in the *T*-α space, which may likely introduce additional uncertainties. For these reasons, defining a water stress iso-line may not be valid. In addition, the soil temperatures or vegetation temperatures at the water stress iso-line show fluctuations that are not physically realistic when compared to changes in values of surface albedo. Therefore, in this study, the water stress iso-line was defined using more pixels, and the resulting soil and vegetation temperatures along this iso-line are then illustrated in the two dimensional plot of surface temperature-albedo (Figure 7).

Figure 7 illustrates the variation in soil and vegetation component temperatures along the water stress iso-line. The soil and vegetation temperatures for all pixels along the iso-line are nearly identical. Based on these results, the performance of component temperatures separated from the composite land surface temperatures derived from ASTER thermal infrared bands verifies a theory of water stress iso-line in the space. The results further indicate that the soil and vegetation component temperatures were successfully separated using the *T*-α space method. Although there were slight temperature fluctuations, they ranged within 1 K, and changes in the soil temperatures on the iso-line were relatively stable, but fluctuations of vegetation temperatures are still relatively larger. The slight fluctuations of soil temperature according to the changes in the surface albedo are reasonable, and the slight fluctuations may be attributed to the uncertainty produced by the process of determining the maximum vegetation in the space. As in the early season, the crops grow extremely quickly, and it is difficult to acquire the withered vegetation pixels from the images with a spatial resolution of 90 m. The limited number of withered vegetation pixels, if they do exist, is likely to cause significant uncertainty in determining the dry edge in the *T*-α space. The relatively large fluctuations of vegetation temperatures can be mainly attributed to the

accuracy of separated soil temperatures and land surface composite temperatures derived from the ASTER images when using Equation (5).

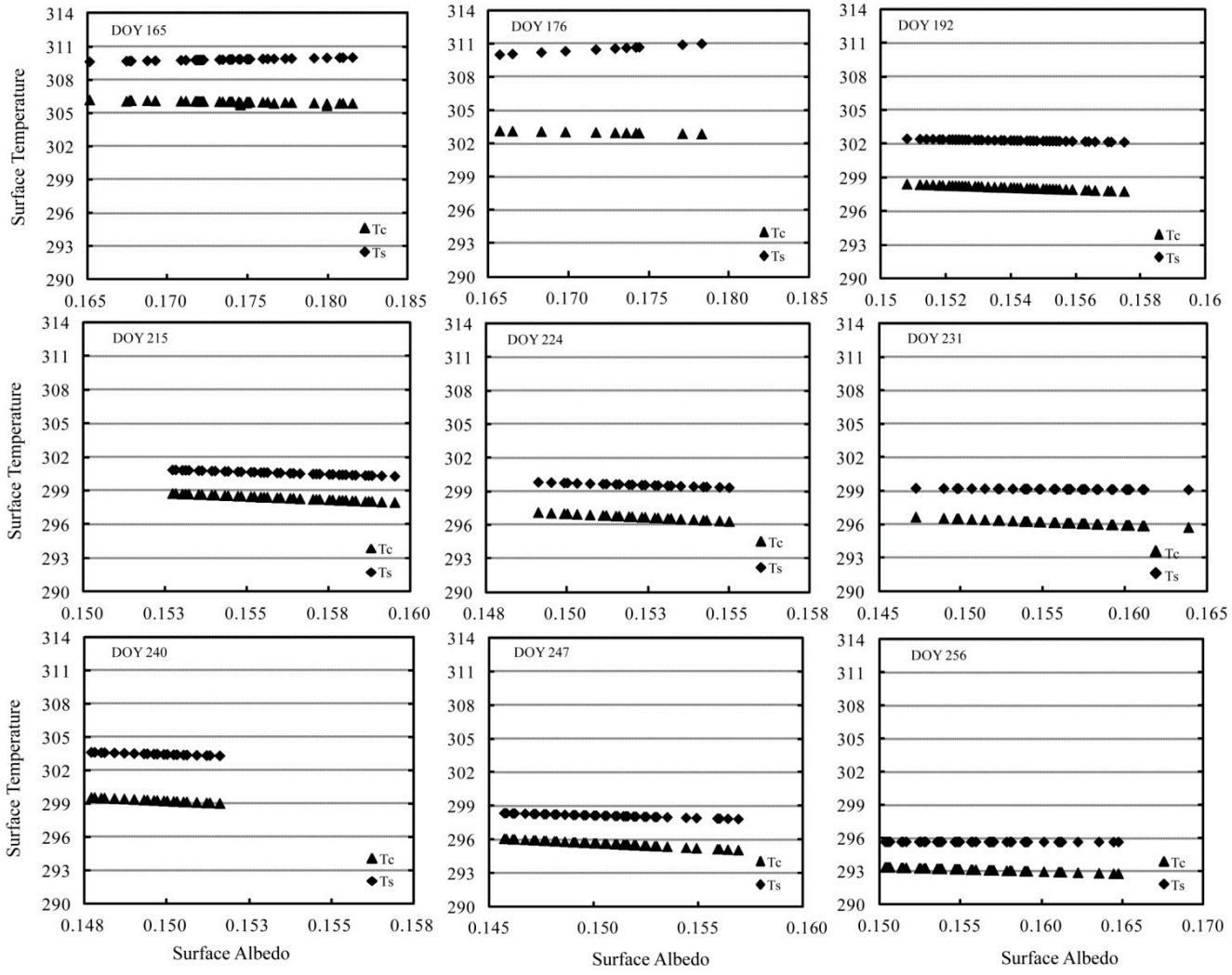

Figure 7. Evaluations in separated soil temperatures and vegetation temperatures at the water stress iso-line at the ASTER overpass times.

6. Conclusions

Developing approaches for separating soil and vegetation component temperatures from multiple or single view angle TIR observations sensors is seen as a major advantage for monitoring plant water use and stress. Multi-VNIR, TIR optimization method, and multi-angle methods have been developed. These methods do not appear capable of providing reliable component temperatures except under certain (limited) conditions. The former method always leads to ill-posed nature equations. Although the later method can remove the ill-posed nature equations during retrieval of the component temperatures, it is far from satisfactory considering the coarse accuracy and complex process and so on. This study proposed using *T*-α space to separate the soil and vegetation component temperatures according to the SEB-1S modeling approach using remote sensing imagery data obtained from satellite sensor with 90 m TIR pixel resolution (ASTER). Finally, the soil and vegetation component temperatures were successfully separated using *T*-α space with analytical geometry with the defined seven end-members

and determining the slopes of the soil moisture iso-lines in the space. This approach is robust, and provides accurate component temperatures at the regional scale, even though the TIR remote sensing data products are mainly from single view angle observation sensors, such as ASTER, Landsat, MODIS, environmental and disaster monitoring and forecasting satellite constellation (HJ-1 Satellite) and so on. The validation in the HiWATER study area demonstrates that reasonable soil and vegetation component temperatures have been derived using the *T*-α space derived from ASTER observations. However, several improvements are foreseen to optimize the separated results and to extend its applicability: (1) there is a considerable need for ground-based soil and vegetation component temperatures at pixel scale to validate the satellite-derived component temperatures; (2) although the methodology using *T*-α space can be operationally applied to irrigated regions surrounded by an arid landscape (oasis areas) using the remote sensing image data, applications for more heterogeneous semiarid areas containing natural vegetation should be examined to see if additional parameterizations are required to obtain reliable results, for example, by introducing the aerodynamic resistance to constrain the minimum vegetation temperature; (3) achieving an accuracy of 1.0 K for land surface temperature from the satellite image data will improve component temperature separation.

The *T*-α space approach derived according to the SEB-1S model was used to estimate soil and vegetation component temperatures from the ASTER TIR and VNIR data. The validations demonstrate a good agreement between the estimated and measured/interpolated soil and vegetation temperatures. For the soil temperatures, the average bias and RMSE values were −0.26 K and 0.83 K, respectively, while for the separated vegetation temperatures, the average bias and RMSE values were −1.29 K and 1.64 K respectively. The derived soil and vegetation temperatures along the selected soil moisture iso-line are equal, though with slight fluctuations. In addition, the derived vegetation temperatures are extremely close to the measured near surface (5 m, above ground level) air temperatures when the remote sensing pixels were nearly full vegetation cover and soil are well. These validations means the proposed *T*-α space approach is appropriate to derive soil and vegetation temperatures from single view angle observations which could improve in estimating the soil evaporation and vegetation transpiration, monitoring crop drought and soil moisture and forecasting climate change at the regional scale.

Acknowledgments

We thank all the scientists, engineers, and students who participated in HiWATER field campaigns. This work was supported by the National Natural Science Foundation of China (91125002) and the National Basic Research Program of China (2015CB953702). We would like to thank Qiang Liu at College of Global Change and Earth System Science, Beijing Normal University. The authors also especially would like to thank Guoyu Qiu at School of Environment and Energy, Shenzhen Graduate School of Peking University for thermal images collected from the thermal camera and Mingsong Li at School of Resources and Environment, University of Electronic Science and Technology of China for supplying ASTER thermal infrared images in study area. We thank the anonymous referees for their constructive criticism and comments.

Author Contributions

Lisheng Song was responsible for implementation of land surface temperature and albedo space method, data preparation, processing and writing of the manuscript. Shaomin Liu was responsible for research design and analysis. William P. Kustas revised the manuscript and gave constructive comments and suggestions. Ji Zhou contributed to ASTER LST data supply and gave constructive comments and suggestions. Yanfei Ma contributed to processing the remote sensing data. USDA is an equal opportunity employer and provider.

Conflicts of Interest

The authors declare no conflict of interest.

References

1. Wan, Z. New refinements and validation of the MODIS Land-Surface Temperature/Emissivity products. *Remote Sens. Environ.* **2008**, *112*, 59–74.
2. Li, Z.; Tang, B.; Wu, H.; Ren, H.; Yan, G. Satellite-derived land surface temperature: Current status and perspectives. *Remote Sens. Environ*. **2013**, *131*, 14–37.
3. Crow, W.; Wood, E. The assimilation of remotely sensed soil brightness temperature imagery into a land surface model using ensemble Kalman filtering: A case study based on ESTAR measurements during SGP97. *Adv. Water Resour*. **2003**, *26*, 137–149.
4. Anderson, M.; Allen, R.; Morse, A.; Kustas, W. Use of Landsat thermal imagery in monitoring evapotranspiration and managing water resources. *Remote Sens. Environ.* **2012**, *122*, 50–65.
5. Kustas, W.; Anderson, M. Advances in thermal infrared remote sensing for land surface modeling. *Agric. For. Meteorol.* **2012**, *149*, 2071–2081.
6. Hansen, J.; Ruedy, R.; Sato, M.; Lo, K. Global surface temperature change. *Rev. Geophys*. **2010**, *48*, RG4004.
7. Merlin, O.; Rudiger, C.; Al Bitar, A.; Richaume, P.; Walker, J.; Kerr, Y. Disaggregation of SMOS soil moisture in southeastern Australia. *IEEE Trans. Geosci. Remote Sen.* **2012**, *50*, 1556–1571.
8. Crow, W.; Kustas, W.; Prueger, J. Monitoring root-zone soil moisture through the assimilation of a thermal remote sensing-based soil moisture proxy into a water balance model. *Remote Sens. Environ*. **2008**, *112*, 1268–1281.
9. Eckmann, T.; Roberts, D.; Still, C. Using multiple endmember spectral mixture analysis to retrieve subpixel fire properties from MODIS. *Remote Sens. Environ*. **2008**, *112*, 3773–3783.
10. Eckmann, T.; Roberts, D.; Still, C. Estimating subpixel fire sizes and temperatures from ASTER using multiple endmember spectral mixture analysis. *Int. J. Remote Sens*. **2009**, *30*, 5851–5864.
11. Jackson, R.; Idso, S.; Reginato, R.; Pinter, P. Canopy temperature as a crop water stress indicator. *Adv. Water Resour*. **1981**,*17*,1133–1138.
12. Zhou, J.; Chen, Y.; Wang, J.; Zhan, W. Maximum nighttime urban heat island (UHI) intensity simulation by integrating remotely sensed data and meteorological observations. *IEEE J-STARS* **2011**, *4*, 138–146.

13. Holmes, T.R.H.; de Jeu, R.A.M.; Owe, M.; Dolman, A.J. Land surface temperature from Ka band (37 GHz) passive microwave observations. *J. Geophys. Res.* ***2009***, *114*, D04113.
14. Zhou, J.; Dai, F.; Zhang, X.; Zhao, S.; Li, M. Developing a temporally land cover-based look-up table (TL-LUT) method for estimating land surface temperature based on AMSR-E data over the Chinese landmass. *Int. J. Appl. Earth Obs*. **2015**, *34*, 35–50.
15. Kimes. D. Remote sensing of temperature profiles in vegetation canopies using multiple view angles and inversion techniques. *IEEE Trans. Geosci. Remote Sens.* **1981**, *19*, 85–90.
16. Zhan, W.; Chen, Y.; Zhou, J.; Li, J. An algorithm for separating soil and vegetation temperatures with sensors featuring a single thermal channel. *IEEE Trans. Geosci. Remote Sens.* **2011**, *49*, 1796–1809.
17. Jia, L.; Li, Z.; Menenti, M.; Su, Z.; Verhoef, W.; Wan, Z. A practical algorithm to infer soil and foliage component temperatures from bi-angular ATSR-2 data. *Int. J. Remote Sens*. **2003**, *24*, 4739–4760.
18. Shi, Y. Thermal infrared inverse model for component temperatures of mixed pixels. *Int. J. Remote Sens*. **2011**, *32*, 2297–2309.
19. Liu, Q.; Yan, C.; Xiao, Q.; Yan, G.; Fang, L. Separating vegetation and soil temperature using airborne multiangular remote sensing image data. *Int. J. Appl. Earth Obs*. **2012**, *17*, 66–75.
20. Soux, A.; Voogt, J.; Oke, T. A model to calculate what a remote sensor "sees" of an urban surface. *Bound Lay Meteorol*. **2004**, *111*, 109–132.
21. Ren, H.; Liu, R.; Yan, G.; Mu, X.; Li, Z.; Liu, Q. Angular normalization of land surface temperature and emissivity using multiangular middle and thermal infrared data. *IEEE Trans. Geosci. Remote Sens.* **2014**, *52*, 4913–4931.
22. Jiang, L.; Islam, S. A methodology for estimation of surface evapotranspiration over large areas using remote sensing observations. *Geophys. Res. Lett*. **1999**, *26*, 2773–2776.
23. Tang, R.; Li, Z.; Tang, B. An application of the Ts-VI triangle method with enhanced edges determination for evapotranspiration estimation from MODIS data in arid and semi-arid regions: Implementation and validation. *Remote Sens. Environ*. **2010**, *114*, 540–551.
24. Merlin, O.; Chirouze, J.; Olioso, A.; Jarlan, L.; Chehbouni, G.; Boulet, G. An image-based four-source surface energy balance model to estimate crop evapotranspiration from solar reflectance/thermal emission data (SEB-4S). *Agric. For. Meteorol.* **2014**, *184*, 188–203.
25. Merlin, O. An original interpretation of the wet edge of the surface temperature-albedo space to estimate crop evapotranspiration (SEB-1S), and its validation over an irrigated area in northwestern Mexico. *Hydrol. Earth Syst. Sci*. **2013**,*17*, 3623–3637.
26. Merlin, O.; Jacob, F.; Wigneron, J.; Walker, J.; Chehbouni, G. Multidimensional disaggregation of land surface temperature using high-resolution red, near-infrared, shortwave-infrared, and microwave-L bands. *IEEE Trans Geosci. Remote Sens.* **2012**, *50*, 1864–1880.
27. Sandholt, I.; Rasmussen, K.; Andersen, J. A simple interpretation of the surface temperature/vegetation index space for assessment of surface moisture status. *Remote Sens. Environ*. **2002**, *79*, 213–224.
28. Carlson, T. An overview of the "triangle method" for estimating surface evapotranspiration and soil moisture from satellite imagery. *Sensors* **2007**, *7*, 1612–1629.
29. Yang, Y.; Shang, S. A hybrid dual-source scheme and trapezoid framework-based evapotranspiration model (HTEM) using satellite images: Algorithm and model test. *J. Geophys. Res. Atmos.* **2013**, *118*, 2284–2300.

30. Zhang, R.; Tian, J.; Su, H.; Sun, X.; Chen, S.; Xia, J. Two improvements of an operational two-layer model for terrestrial surface heat flux retrieval. *Sensors* **2008**, *8*, 6165–6187.
31. Long, D.; Singh, V. A Two-source trapezoid model for evapotranspiration (TTME) from satellite imagery. *Remote Sens. Environ*. **2012**, *121*, 370–388.
32. Li, X.; Cheng, G.; Liu, S.; Xiao, Q.; Ma, M.; Jin, R.; Che, T.; Liu, Q.; Wang, W.; Qi, Y.; *et al.* Heihe watershed allied telemetry experimental research (HiWATER): Scientific objectives and experimental design. *Bull. Am. Meteorol. Soc*. **2013**, *94*, 1145–1160.
33. Xu, Z.; Liu, S.; Li, X.; Shi, S.; Wang, J.; Zhu, Z.; Xu, T.; Wang, W.; Ma, M. Intercomparison of surface energy flux measurement systems used during the HiWATER-MUSOEXE. *J. Geophys. Res.* **2013**, *118*, 13140–13157.
34. Li, H.; Sun, D.; Yu, Y.; Wang, H.; Liu, Y.; Liu, Q.; Du, Y.; Wang, H.; Cao, B. Evaluation of the VIIRS and MODIS LST products in an arid area of Northwest China. *Remote Sens. Environ.* **2013**, *142*, 111–121.
35. Song, L.; Liu, S.; Zhang, X.; Zhou, J.; Li, M. Estimating and validating soil evaporation and crop transpiration during the HiWATER-MUSOEXE. *IEEE Geosci. Remote Sens*. **2015**, *12*, 334–338.
36. Sánchez, J.; Kustas, W.; Caselles, V.; Anderson, M. Modelling surface energy fluxes over maize using a two-source patch model and radiometric soil and canopy temperature observations. *Remote Sens. Environ*. **2008**, *112*, 1130–1143.
37. Montandon, L.; Small, E. The impact of soil reflectance on the quantification of the green vegetation fraction from NDVI. *Remote Sens. Environ*. **2008**, *112*, 1835–1845.
38. Jiang, Z.; Huete, A.; Chen, J.; Chen, Y.; Li, J.; Yan, G.; Zhang, X. Analysis of NDVI and scaled difference vegetation index retrievals of vegetation fraction. *Remote Sens. Environ*. **2006**, *101*, 366–378.
39. Gebremichael, M.; Barros, A. Evaluation of MODIS Gross Primary Productivity (GPP) in tropical monsoon regions. *Remote Sens. Environ*. **2006**, *100*, 150–166.
40. Zeng, X.; Dickinson, R.; Walker, A.; Shaikh, M.; DeFries, R.; Qi, J. Derivation and evaluation of global 1-km fractional vegetation cover data for land modeling. *J. Appl. Meteorol. Clim*. **2000**, *39*, 826–839.
41. Jiménez-Muñoz, J.C.; Sobrinoa, J.A.; Gillespie, A.; Sabol, D.; Gustafson, W. Improved land surface emissivities over agricultural areas using ASTER NDVI. *Remote Sens. Environ*. **2006**, *103*, 474–487.
42. Sobrino, J.; Jiménez-Muñoz, J.; Paolini, L. Land surface temperature retrieval from LANDSAT TM 5. *Remote Sens. Environ*. **2004**, *90*, 434–440.
43. Zhou, J.; Li, M.; Liu, S.; Jia, Z.; Ma, Y. Validation and performance evaluations of methods for estimating land surface temperatures from ASTER Data in the middle reach of the Heihe River Basin, Northwest China. *Remote Sens*. **2015**, under review.
44. Liang, S. Narrowband to broadband conversions of land surface albedo I: Algorithms. *Remote Sens. Environ*. **2001**, *76*, 213–238.
45. Stisen, S.; Sandholt, I.; Nørgaard, A.; Fensholt, R.; Jensen, K. Combining the triangle method with thermal inertia to estimate regional evapotranspiration—Applied to MSG-SEVIRI data in the Senegal River basin. *Remote Sens. Environ*. **2008**, *112*, 1242–1255.

46. Guillevic, P.; Biard, J.; Hulley, G.; Privette, J.; Hook, S.; Olioso, A.; Göttschee, F.; Radocinski, R.; Román, M.; Yu, Y.; *et al.* Validation of land surface temperature products derived from the visible infrared imaging radiometer suite (VIIRS) using ground-based and heritage satellite measurements. *Remote Sens. Environ*. **2014**, *154*, 19–37.
47. Duan, S.; Li, Z.; Wang, N.; Wu, H.; Tang, B. Evaluation of six land-surface diurnal temperature cycle models using clear-sky *in situ* and satellite data. *Remote Sens. Environ*. **2012**, *124*, 15–25.
48. Göttsche, F.; Olesen F. Modelling of diurnal cycles of brightness temperature extracted from METEOSAT data. *Remote Sens. Environ*. **2001**, *76*, 337–348.